Fenton chemistry-based detemplation of an industrially relevant microcrystalline beta zeolite. Optimization and scaling-up studies.

María J. Ortiz-Iniesta and Ignacio Melián-Cabrera*

Chemical Reaction Engineering, Institute of Technology & Management, University of Groningen, Nijenborgh 4, 9747 AG Groningen, The Netherlands.

* Corresponding Author:

i.v.melian.cabrera@rug.nl (Ignacio Melián Cabrera)

Abstract

A mild template removal of microcrystalline beta zeolite, based on Fenton chemistry, was optimized. Fenton detemplation was studied in terms of applicability conditions window, reaction rate and scale up. TGA and CHN elemental analysis were used to evaluate the detemplation effectiveness, while ICP, XRD, LPHR-Ar physisorption, and ^{27}Al MAS NMR were applied to characterize the structure and texture of the resulting materials. The material properties were compared to calcination. By understanding the interplay of relevant parameters of the Fenton chemistry, the process can be optimized in order to make it industrially attractive for scale-up. The H_2O_2 utilization can be minimized down to 15 mL H_2O_2/g (88 °C, 30 ppm Fe), implying a high solid concentration and low consumption of H_2O_2. When Fe concentration must be minimized, values as low as 5 ppm Fe can be applied (88 °C, 30 mL H_2O_2/g), to achieve full detemplation. The reaction time to completeness can be reduced to 5 h when combining a Fe-oxalate catalyst with UV radiation. The protocol was scaled up to 100 times larger its original recipe. In terms of the material's properties, the scaled material is structurally comparable to the calcined counterpart (comparable Si/Al and XRD patterns), while it displays benefits in terms of texture and Al-coordination, the latter with full preservation of the tetrahedral Al.

Keywords

> Zeolite beta
> Calcination
> Template removal
> Fenton chemistry
> Dealumination

1. Introduction

Progress in relevant areas of oil-refining, petrochemistry, fine chemicals and pollution abatement can be attributed to zeolites [1-6]. Zeolites are microporous crystalline aluminosilicates that have many exploitable properties such adsorption, separation and catalysis. They are typically synthesized at specific conditions with very precise gel compositions [7]. Often hydrothermal conditions are necessary to provoke the nucleation and crystal growth in the presence of mineralizers, such as NaOH, $NaAlO_4$ or fluoride compounds.

Among the various synthetic approaches, the use of organic structural directing agents (SDA) has been crucial to discovering new zeolites [8-13]. This was possible due to the introduction of quaternary and diquaternary alkyl ammonium compounds, amines, alkylphosphonium salts and phosphazenes, among the most relevant ones. The removal of these SDA molecules is an essential step in order to obtain the final porous network. This step is normally carried out by calcination of the dried gel at temperatures ranging 500 up to 650 °C [3,4]. For the case of ill-crystalline zeolites, having crystal sizes below 1 μm, such type of calcination is problematic. The inorganic network is unstable, in particular when the Al concentration is high. This is caused by the longer distance of the Al-O bonds that makes it easily to be hydrolysed in the presence of the self-generated steam during calcination. This is the case of beta zeolite [14-16]. Recent advances in beta zeolite synthesis are in the direction of template-free routes and some remarkable examples have been reported [17-19]. However, the current industrial manufacturing process of beta zeolite still involves tetraethyl-ammonium hydroxide (TEA) as SDA; the organic template seems to be crucial to control the crystal growth. However, the removal of the TEA by calcination in zeolite beta is known to have serious drawbacks; the most remarkable is the dealumination with the formation of extra framework species [20-23].

Therefore, it has been a challenge to find alternative routes to detemplate beta zeolite at milder conditions.

Studies on solvent extraction of SDAs by Davis and co-workers reported that successful extraction is limited to the case that the SDA has a smaller size than the pore opening of the zeolite, and secondly, weak interactions with the zeolite framework [24]; in the case of Al-beta zeolite around 50% of the template could be extracted. Solvent extraction applied to a colloidal beta zeolite removed most of the SDA, and ~65% of the microporosity was developed [25]. Cold plasma has been successfully applied to nano-sized beta zeolite, with full template removal and structural preservation. The acidic properties, density and strength, for the plasma-derived route were lowered when compared to the calcined route [26]. In parallel to these studies, a mild detemplation method based on highly-oxidizing $OH^{\bullet}$ radicals to decompose the SDA of a microcrystalline beta zeolite was proposed by Melián-Cabrera *et al.* [27-29]. More recently, the approach was extended to a soft MCM-41 [30] and SBA-15 [31]. This methodology has been successfully applied to mesoporous silicates and aluminosilicates [32,33], RUB-18 [34], aluminophosphates [35,36], silicalite-1 colloids, and transparent composite film containing zeolite nanoparticles for organic light emitting devises [37]. A simultaneous detemplation and metal introduction method has been reported as well [38-40]. A simplified route using H_2O_2 in the absence of Fe has been successfully applied to mesoporous silicates such as MCM-56 [41], regeneration of Al-doped ZSM-5 membranes [42], and silicoalumina phosphates (SAPO-34) [36]. Other attempts to generate $OH^{\bullet}$ radicals from H_2O_2 were assisted by UV light radiation to detemplate SBA-15 [43], and microwave irradiation over nano-beta particles [44] and AlPO-5 [45].

Fenton chemistry-based detemplation consists of using $OH^{\bullet}$ radicals as oxidizing agents to remove the organic templates in zeolites, zeotypes and mesopororous materials. These radicals are normally originated from the catalytic decomposition of H_2O_2 at low

temperature, using a Fe salt as catalyst at ppm level, though it can be assisted by UV radiation. In order to make this approach industrially attractive for zeolite activation, there are a number of aspects that require careful consideration. In this work we have carried out systematic studies considering those practical aspects, such as: the influence of relevant parameters on detemplation (temperature, Fe concentration and H_2O_2 utilization), optimization about reducing the utilization of H_2O_2 and Fe concentration, reduction of the reaction time aided by UV irradiation, an scaling-up investigation and the evaluation of relevant properties for the derived scaled-up material. These investigations have been carried out on an industrially relevant zeolite beta.

2. Experimental

2.1. Materials

Stabilized hydrogen peroxide (30 *wt.*% H_2O_2 in H_2O), nitric acid, (65 *wt.*%, pro analysi) and ammonia solution (25 *wt.*%, pro analysi) were purchased from Merck. Non-stabilized hydrogen peroxide (30 *wt.*% H_2O_2 in H_2O) was purchased from Sigma-Aldrich. $Fe(NO_3)_3 \cdot 9H_2O$ (98 %, metal basis, denoted as Fe^{III}-nitrate) and $(NH_4)_3[Fe(C_2O_4)_3] \cdot 3H_2O$ (pure, denoted as Fe^{III}-oxalate) were supplied by Riedel-de-Haën. NH_4-templated beta zeolite (HSZ-930A) were purchased from TOSOH Corporation.

2.2. Detemplation protocols

2.2.1. Calcination

The general calcination procedure was carried out in a LT9/11 Nabertherm box furnace. The samples were loaded in porcelain crucibles in shallow bed configuration, heated from 30 to 550 °C at 5 °C/min and held at 550 °C for 6 h.

2.2.2. Fenton chemistry-based detemplation

Standard experiment: 0.5 g of raw zeolite was mixed with the desired amount (15 mL) of 30% H_2O_2 (stabilized or non-stabilized; non-stabilized was used for temperatures ≤70 °C)

and stirred until the mixture was homogeneous. Then, the chosen concentration of Fe was adjusted. In the standard experiment 30 mg Fe/Kg (referred as ppm) was used. This concentration was obtained by adding 65 µL of a stock solution (5 g Fe^{III}-nitrate or 5.28 g Fe^{III}-oxalate in 100 mL of deionised water). The pH was adjusted to 4 using diluted HNO_3. The flask containing the reaction mixture was submerged in a pre-heated oil bath at the desired temperature (79 °C in this case) and it was maintained for 24 h under stirring and refluxing to prevent evaporation. The solid was separated by centrifugation, washed with deionised water and dried overnight at 80°C in a stove oven. In other cases, the pH of the resulting mixture was below 4 and it was adjusted using a diluted NH_3 solution.

Optimization studies: For the optimization studies, temperature was evaluated from room temperature to 90 °C, the Fe concentration from 0 to 60 ppm, and H_2O_2 utilisation from 10 to 90 mL/g. The influence of the H_2O_2 type was investigated using stabilized and non-stabilized H_2O_2. The pH was adjusted with either diluted HNO_3 or NH_3 depending on the applied Fe ppm and H_2O_2 utilization. For the evaluation of the dominant parameters, boundary conditions were selected according to Table 1.

Kinetic study: In the time-dependency pseudo-kinetic study, Fe^{III}-nitrate and Fe^{III}-oxalate were used as precursors; the concentration was fixed at 30 and 60 ppm and reaction times ranged from 1 to 20 h. Individual experiments were performed for each reaction time. A water-bath was used to keep the reaction temperature constant at 70 °C.

Photo-Fenton: The experiments assisted with UV-light (5.5 W Hg lamp) were performed in a commercial set-up (Aceglass, 7880-60) which was modified for this purpose. The preparation of the reaction mixture follows the same procedure than the standard protocol detailed above. In this case, two Fe sources were employed: Fe^{III}-nitrate and Fe^{III}-oxalate. The reaction time was ranged between 1 and 8 hours.

Scale-up experiment: 16.67 g of zeolite were mixed with 500 mL of stabilized H_2O_2 and 2.166 mL of Fe^{III}-nitrate stock solution (5 g Fe^{III}-nitrate in 100 mL of deionised water), and the standard protocol described above was followed.

2.3. Characterization

Thermogravimetric analyses (TGA) were carried out in a Mettler-Toledo (TGA/SDTA851e) analyser using a flow of synthetic air of 80 mL/min (NTP). Typically, 5-10 mg of sample was loaded in a 70 μL α-Al_2O_3 crucible and the temperature was increased from 30 to 900 °C at 10 °C/min. Blank curve correction using an empty crucible was subtracted.

CHN elemental analyses were carried out in a EuroVector 3000 CHNS analyzer. All analyses were done in duplicate to check sample heterogeneity; the standard deviation was below 2 *wt.*% Approximately 2 mg of sample were accurately weighed in a 6-digit analytic balance (Mettler-Toledo). The samples were burned at 1800 ºC in the presence of an oxidation catalyst and decomposed into CO_2, H_2O and N_2. These gases were then separated in a Porapak QS column at 80 °C and quantified with a TCD detector. Acetanilide (99.9 %, Heka Tech) was used as external standard.

Inducted coupled plasma atomic emission spectroscopy (ICP-AES) analyses were carried to determine the Si/Al ratio and the concentration of residual Fe in the samples. To that effect, a known amount of solid sample was dissolved in a 6 *wt.* % HF solution overnight to ensure complete dissolution. The liquid concentration was determined in a Perkin-Elmer (Optima 7000 DV) instrument.

Powder X-ray diffraction (XRD) spectrum were collected with a Bruker D8 powder X-ray diffractometer using CuKα radiation, λ=1.54056 Å. The spectra were recorded with a step size of 0.02°; 3 seconds (s) accumulation time and in the 2θ angle range of 5-60°.

Textural analyses were carried out by Ar physisorption at -186 °C, in a Micromeritics ASAP 2020. Prior to the measurements, the samples were outgassed under

vacuum at 300 ºC for 12 h. The Fenton-derived materials were degassed at 150 ºC. The surface area was calculated by BET method (S_{BET}). The single point pore volume (V_T) was estimated from the amount adsorbed at a relative pressure of ~0.98 in the desorption branch. The micropore parameters were determined from the *t*-plot model, cumulative pore volume and surface area. The pore size distribution was determined from the Horvath-Kawazoe differential model.

^{27}Al magic angle spinning nuclear magnetic resonance (MAS-NMR) measurements were conducted on a Bruker Avance-400 spectrometer using a 4 mm zirconium holder, applying spinning frequency of 11 kHz at 25 °C. The ^{27}Al MAS NMR spectra were obtained at 104.201 MHz, with acquisition delay of 1 s and acquisition time of 0.08 s. typically 4000 scans were collected. The spectra were referenced with respect to 1.0 M aqueous solution of $Al(NO_3)_3$ set on 0 ppm.

2.4. Definitions

TGA-based detemplation efficiency:

$$\eta^{TGA}\,(\%) = \left[1 - \frac{TGA_{200-900}(\text{sample}) - Wo}{TGA_{200-900}(\text{raw}) - Wo}\right] \times 100 \qquad (1)$$

where $TGA_{200\text{-}900}$(sample) is the TGA weight loss between 200 and 900 °C for any sample, $TGA_{200\text{-}900}$(raw) is the TGA weight loss for the zeolite containing the template and *W*o is the TGA weight loss of a reference material consisting of a fully detemplated beta zeolite where full detemplation was confirmed by carbon elemental analysis. *W*o corresponds to the experiment using 30 mL H_2O_2/g, 30 Fe ppm at 70 °C for 24 h (scale-up experiment). This weight loss has two contributions; first, the condensation of the silanol groups, which condensate at temperatures > 300 °C. And secondly, residual NH_4 groups after detemplation, available in the original zeolite (NH_4-form). During TGA experiments, these

groups release at temperatures > 300 °C, contributing to *Wo* as well. Thus, this parameter will account for the release of dehydroxylation water and residual NH_4-groups.

CHN-based detemplation efficiency:

$$\eta^{C}(\%) = \left[1 - \frac{C_{CHN}(\text{sample})}{C_{CHN}(\text{raw})}\right] \times 100 \quad (2)$$

Where C_{CHN}(sample) is the carbon content determined by elemental analysis of the material under study and C_{CHN}(raw) is the carbon content of the raw material (BT-*raw*) determined in the same way.

Mesopore volume:

$$V_{MESO}^{t-plot}\ (cm^3/\text{g}) = V_T\ -\ V_{\mu}^{t-plot} \quad (3)$$

Where V_T (cm^3/g) is the total pore volume and V_{μ}^{t-plot} is the corresponding micropore volume according to the *t*-plot model:

$$r(\text{Å}) = \left[\frac{13.99}{0.034 - log\left(\frac{p}{p_0}\right)}\right]^{1/2} \quad (4)$$

Mesopore surface area:

$$S_{MESO}^{t-plot}\ (m^2/\text{g}) = S_{BET} -\ S_{\mu}^{t-plot} \quad (5)$$

Where S_{BET} (m^2/g) is the specific surface area determined by the BET model and S_{μ}^{t-plot} is the corresponding micropore surface area for pores ≤ 20 Å, determined by the *t-plot* model (eq. 4).

Fe adsorption:

$$\text{Fe}^{ADS}(\%) = \left[\frac{\text{Fe}^{ICP}(\text{material}) - \text{Fe}^{ICP}(\text{calcined})}{\text{Fe (applied Fenton solution)}}\right] \times 100 \quad (6)$$

Where Fe^{ICP}(material) is the concentration of Fe measured on the dried material after Fenton detemplation by ICP, Fe^{ICP}(calcined) is the measured ICP value for the BT-*C*

calcined material, which contains Fe impurities, and Fe(applied Fenton solution) is the applied Fe concentration of the solution used to catalyse the Fenton reaction.

3. Results and discussion

3.1. Influence of relevant detemplation parameters

The kinetics of Fenton reaction are known to be dependent on several parameters [46-48]: reactor geometry and scale, temperature, concentration of Fe and H_2O_2, pH, stirring and addition modes. The first step in the optimization of this procedure was to determine which variables are relevant for zeolite detemplation. Thus, the influence of the temperature, Fe concentration and H_2O_2 utilisation was investigated. Preliminary experiments were performed to test the reaction scale (between 5 and 15 mL) and reactor geometry (cylinder or bulb); and no substantial differences on the detemplation level were found, as long as the temperature was well controlled. The pH was adjusted at the beginning of the reaction for all the experiments; and the parameters related to the experimental protocol such as stirring rate and addition mode were kept constant. Subsequently, the additional experimental parameters for optimisation were chosen: reaction temperature, H_2O_2 utilization (mL per gram of zeolite) and Fe concentration.

In order to determine how these parameters affect the detemplation level, a model based on the Hadamard design was applied [49,50]. This model is based on experimental values and it provides the level of influence of each parameter. Despite it is a relatively simple model, the dependency between parameters is not considered. Once the variables were defined, the range (*i.e.* minima and maxima) has to be determined experimentally. These values will determine the barriers where the model works. The experimental conditions of the four experiments (denoted as H1, H2, H3 and H4) are given in Table 1. In this Hadamard design, the influence of three chosen variables was studied on the level of zeolite detemplation. The following equations (7-10) were solved:

$$y_1 = \theta_0 + \theta_1 + \theta_2 + \theta_3 + e_1 \quad (7)$$

$$y_2 = \theta_0 + \theta_1 - \theta_2 - \theta_3 + e_2 \quad (8)$$

$$y_3 = \theta_0 - \theta_1 + \theta_2 - \theta_3 + e_3 \quad (9)$$

$$y_4 = \theta_0 - \theta_1 - \theta_2 + \theta_3 + e_4 \quad (10)$$

where y_1, y_2, y_3 and y_4 are the experimental values of the parameter to be optimized; θ_1, θ_2 and θ_3 are the values of the parameters P_1, P_2 and P_3, respectively; and θ_0 is their average value. The associated errors are e_1, e_2, e_3 and e_4. The estimated values θ_0, θ_1, θ_2 and θ_3 are applied in Eq. (11) being Y the parameter to be optimized (degree of detemplation).

$$Y = \theta_0 + \theta_1 P_1 + \theta_2 P_2 + \theta_3 P_3 \quad (11)$$

For this set of experiments, the 4×4 Hadamard matrix was defined according to equations (12-15):

$$99 = \theta_0 + \theta_1 + \theta_2 + \theta_3 + e_1 \quad (12)$$

$$19 = \theta_0 + \theta_1 - \theta_2 - \theta_3 + e_2 \quad (13)$$

$$25 = \theta_0 - \theta_1 + \theta_2 - \theta_3 + e_3 \quad (14)$$

$$37 = \theta_0 - \theta_1 - \theta_2 + \theta_3 + e_4 \quad (15)$$

that were solved as:

$$Y = 48.8 + 17.3 P_1 + 16.8 P_2 + 23.3 P_3 \quad (16)$$

All the parameters have positive coefficients, meaning that their increase would imply a detemplation improvement. Quantitatively, very similar influence was found for the reaction temperature (P_1) and H_2O_2 utilisation (P_2): 17.3 and 16.8, respectively. Remarkably, the Fe concentration (P_3) showed the largest influence, 23.3. However, from the practical point of view, increasing the Fe concentration excessively would be negative in terms of the purity of the final material and acidity, since Fe ions will replace H^+ on the Brønsted sites. Incrementing the amount of H_2O_2 is also detrimental to the final process

costs. Temperature seems to be the way to enhance further the detemplation level. This approach was applied systematically in the forthcoming study.

3.2. Experimental optimization

The fundamentals of Fenton chemistry have been studied for the treatment of residual water and soils. It consists of the decomposition reaction of H_2O_2 in the presence of Fe^{II} to generate hydroxyl radical ($OH^{\bullet}$), eq. 17; then, the reduction of Fe^{III} with H_2O_2 produces new Fe^{II} (eq. 18) that closes the cycle:

$$H_2O_2 + Fe^{2+} \rightarrow OH^{\bullet} + OH^{-} + Fe^{3+} \quad (17)$$

$$H_2O_2 + Fe^{3+} \rightarrow HO_2^{\bullet} + H^{+} + Fe^{2+} \quad (18)$$

The hydroxyl radical reacts with organic compounds with bimolecular rate constants as high as 10^7 to 10^{10} L/mole·sec [46-48,51]. Besides the main reactions, other competing reactions occur as well:

$$RH + OH^{\bullet} \rightarrow H_2O + R^{\bullet} \quad (19)$$

$$OH^{\bullet} + Fe^{2+} \rightarrow OH^{-} + Fe^{3+} \quad (20)$$

$$R^{\bullet} + Fe^{3+} \rightarrow Fe^{2+} + products \quad (21)$$

$$R^{\bullet} + OH^{\bullet} \rightarrow ROH \quad (22)$$

$$R^{\bullet} + H_2O_2 \rightarrow ROH + OH^{\bullet} \quad (23)$$

$$HO_2^{\bullet} + Fe^{3+} \rightarrow O_2 + Fe^{2+} + H^{+} \quad (24)$$

$$OH^{\bullet} + H_2O_2 \rightarrow HO_2^{\bullet} + H_2O \quad (25)$$

Where RH represents the substrate to be oxidised, $R^{\bullet}$ is an organic radical (derived from the RH substrate) and $HO_2^{\bullet}$ is the superoxide radical. The rate constant of the equations 18, 21 and 24 are also pH dependent [52]. As a result of the high reaction kinetic constants, second order and complexity of side reactions, temperature, Fe concentration and H_2O_2 utilisation require optimization.

The focus of this optimization is to find suitable conditions to enable the application of this process on a larger scale. It means using the lowest possible H_2O_2 utilization and Fe concentration, the latter for proper temperature control due to the exothermic and radical reaction, and prevent acid site density depletion. Therefore, an experimental screening study varying the H_2O_2 utilization, Fe concentration, temperature and reaction time was carried out; using two types of H_2O_2, stabilized and non-stabilized.

The determination of the detemplation level was carried out by TGA as analysis technique of choice. In order to confirm the TGA results, control experiments by CHN elemental analysis were performed as well, in the raw and selected resulting materials. For detemplation levels >95% there was no correlation between TGA (η^{TGA}) and CHN (η^{CHN}), Fig. S-1. Possibly because the techniques are near the detection limit, since the materials under analysis possess a low organic content. It was assumed that for η^{CHN} or $\eta^{TGA} \geq 95\%$ full template removal can be considered.

The results from this study are compiled in Table 2, where some general trends can be observed. Reaction temperature, H_2O_2 utilisation and Fe concentration have a positive effect on the detemplation level. These results are consistent with the theoretical findings derived from the Hadamard design.

At low temperatures, RT and 40 °C, stabilised H_2O_2 did not show much detemplation (data not shown). For comparison, non-stabilised H_2O_2 was employed in this range and it showed detemplation values up to 37%. At higher temperatures such as 70 °C, the use of *non*-stabilised H_2O_2 brought also some benefits such as the reduction of H_2O_2 utilisation from 30 to 20 mL (30 h reaction, 30 ppm of Fe), and the Fe concentration from 30 to 10 ppm (30 mL H_2O_2/g, 24 h reaction), achieving a 97 and 98% detemplation respectively. The attained benefits of the *non*-stabilised H_2O_2 likely come from the absence of stabilizers, usually phosphates. The stabilizers can precipitate Fe cations ($FePO_4 \cdot 2H_2O$,

pKs = 15 [53]) and consequently, Fe will suffer a reduction on its effective concentration in solution.

It was generally found that temperature can compensate Fe concentration. At 30 mL/g H_2O_2 utilisation when temperature is increased from 70 to 79 °C, the Fe concentration can be lowered to half (30 to 15 ppm) to achieve a 91 % detemplation. While at 88 °C, only 5 ppm were needed to achieve full detemplation. A similar trend was observed at 15 mL/g H_2O_2 utilization and 30 ppm of Fe: the detemplation improved from 40% at 70 °C to 95% at 88 °C.

A trend between H_2O_2 utilization and temperature was observed as well. At 70 and 79 °C 30 ml of H_2O_2/g are required for full detemplation (30 ppm Fe), while at 88 °C it can be reduced to 20 mL/g (97%, 15 ppm Fe) and 15 mL/g (95%, 30 ppm Fe). It indicates also that under isothermal conditions, there is interplay between H_2O_2 and Fe concentration: a reduction in H_2O_2 requires an increase in Fe concentration. This was just discussed at 88 °C. At 70 °C, the H_2O_2 utilization can be reduced from 30 to 20 mL/g by increasing the Fe concentration from 10 to 30 ppm. A similar effect occurs at 79 °C, 30 to 20 mL H_2O_2/g with an increase of 15 to 30 ppm Fe, though in this case the detemplation was partial (~90%).

Control experiments, where no Fe was added, were performed for comparison. The same temperature dependency was observed but reaching a maximum of 48% detemplation at the highest applied temperature, 88 °C. The presence of partial detemplation in these cases may be due to the combination of two factors: H_2O_2 is an oxidant by itself (E^0=1.77 eV) [53], and the possible catalytic effect of Fe impurities present in the zeolite [54,55]. These blank experiments show that the addition of Fe as catalyst is crucial to achieve full detemplation on zeolite beta.

An important parameter for the final sample purity is the applied Fe concentration. Fe could be reduced from 30 to 10 ppm at 70 °C, using non-stabilized H_2O_2, with full

detemplation using 30 ml H_2O_2/g of zeolite. At 79 °C, the Fe concentration could not be reduced, while at 88 °C the Fe concentration could be decreased to 15 ppm (20 ml/g) or 5 ppm (30 ml/g).

In summary, from the optimization study two set of conditions seem to be appealing for large-scale application of this methodology. When the H_2O_2 needs to be reduced, the optimal conditions were found at 88 °C using 15 ml/g and 30 ppm Fe, which means a relatively high solid concentration (6.25 *wt.*%) and low consumption of H_2O_2. If Fe should be limited in the final zeolite product composition, optimal conditions are found at 88 °C, 30 ml/g and 5 ppm Fe.

3.3. Kinetic study

Additional studies using Fe concentrations of 30 and 60 ppm at different reaction times but at fix temperature (70 °C) and pH (4) were performed in order to understand the kinetic influence of the concentration, Fe source and UV-assistance. The results are given as detemplation level (η^{TGA}) as a function of the reaction time in Figure 1. A clear effect was observed when the Fe concentration was increased; the reaction time to achieve full detemplation was shortened from 20 to 8 hours.

Looking at the TGA patterns of partially detemplated materials (Fig. 2), an additional decomposition peak (step IV) centred at *ca.* 130 °C was observed, that is absent in the raw zeolite decomposition. This temperature is lower than the template decomposition peaks (steps II and III) of the raw material (BT-*raw*) and higher than adsorbed water (step I). According to reported thermal analysis studies [56], step IV can be assigned to oxalate group decomposition. Oxalates are commonly formed during Fenton oxidation of aliphatic-based compounds [48]. Under the presence of Fe, the formation of Fe-oxalate complexes during the process would be favourable thermodynamically, due to their high stability constants (log K_1 (Fe^{II}-oxalate) > 4.7; log K_1 (Fe^{III}-oxalate) = 9.4 [53]).

Therefore, the TGA observation suggests the presence of Fe-oxalates. In order to understand if Fe-oxalate complexes play a role, Fe^{III}-oxalate was directly used as Fe-source. The results are shown in Figure 1. A reduction in the reaction time to achieve full detemplation was observed, from 20 to 15 hours. This enhancement is an indication on the favourable role of stabilizing Fe by complexation during the detemplation.

According to the literature [48,57-60], UV light radiation assists the Fenton reagent in the decomposition of aromatic and aliphatic compounds, leading to higher yields and faster reaction rates. Furthermore, Sulzberger *et al.* reported that UV light in combination with Fe-oxalate complexes give a higher efficiency than using other Fe salts [59,60]. Considering this background information, light-assisted reactions were carried out using Fe-oxalate and Fe-nitrate (30 ppm in both cases). The results are shown in Figure 1. According to our expectations, the reaction time to achieve full detemplation was notably reduced from 15 to 5 hours by combining UV-light and Fe-oxalate; and from 24 to 8 hours combining UV-light and Fe-nitrate as the Fe source.

3.4. Scale up

After investigation on the experimental window where the Fenton chemistry works optimally for the detemplation of such an industrially-relevant beta zeolite, the experiment was scaled up. For that purpose, the following conditions were applied: 30 mL H_2O_2/g, temperature 70 °C and 30 ppm of Fe.

The scale was progressively increased from 5 mL to 500 mL, through 30 and 200 mL. Full detemplation was achieved in all the cases. As example, the TGA pattern for the 500 mL-scale is shown in Fig. 3. It consists of a pronounced weight loss at *ca.* 100 °C due to water desorption and a secondary weight loss at *ca.* 350 °C due to the release of NH_4 groups [28], that is absent in the calcined material. The template removal was confirmed via CHN

elemental analysis, where less than a 0.05% of elemental C was found, see BT-*fsu* in Table 3 for the 500 mL-scale experiment, indicating a detemplation efficiency > 99%.

3.5. Material properties

3.5.1. Structure and composition

The structural characteristics of the Fenton-scaled beta zeolite was analysed by XRD and compared to the calcined counterpart (Fig. 4). The XRD profile of Beta zeolite is a combination of sharp and broad diffractions as a result of the intergrowth of the polymorphs A and B. Both materials show the typical diffractions for BEA structure. Based on the XRD patterns, no substantial structural differences were observed after the Fenton-based treatment compared to calcination.

ICP elemental analysis was performed in order to quantify a possible dealumination due to the acidic medium applied during the Fenton detemplation process (Table 3). Analyses show negligible variation of the Si/Al ratio for BT-*C,* BT-*f* and BT-*fsu,* with a Si/Al ratio ranging 12.4 to 13.5. The Fe content in the final dried solids was measured, in order to evaluate the Fe adsorption during the Fenton detemplation. For that purpose, equation (6) described in the experimental section was employed. In the calcined BT-*C*, Fe traces were found (0.01 *wt*.%). During the Fenton treatment, a substantial part of the applied Fe was adsorbed, ranging 64 and 83% of the applied Fe in solution, rising the absolute values up to 0.1 *wt*.%.

3.5.2. Textural properties

Low-pressure high-resolution Ar physisorption (LPHR-Ar) measurements were performed in order to determine the porosity of the materials under study. The shape of the isotherms (Fig. 5) shows the interaction between adsorbent (Ar) and zeolite surface [16,61]. The adsorption/desorption isotherms correspond to a typical nano-sized Beta zeolite isotherm [16,62-64]. Both materials exhibit a shape of type IV with a type H3 hysteresis loop in the

mesopores region according to the IUPAC classification [65]. This isotherm profile is characteristic of multilayer adsorption with capillary condensation in the mesopores. H3 type loop is observed when small particles aggregate giving rise to slit-shaped pores [65]. At the micropores region (p/p_o<0.3) BT-*fsu* shows higher adsorption; it agrees with the *t*-plot calculations as discussed later. A slight rise of adsorption was observed in the mesopores range 0.3<p/p_o<0.4 followed by two capillary rises: one broad in the range 0.4<p/p_o<0.85 and another near 0.9. The range covered by the desorption hysteresis loop of BT-*fsu* is comparable to the BT-*C*.

Argon physisorption derived *t*-plot (Figure 6) shows an increase in the intercept on the y ordinate. A positive intercept corresponds to the presence of micropores. Consequently, the micropore volume was enhanced by using mild detemplation (BT-*fsu*) instead of calcination (BT-*C*). The overall textural parameters are collected in Table 4. BT-*fsu* has a higher BET surface area; the rise comes from an increase in the micro- and mesoporous contributions, with a higher contribution of the micropores to the increase (~15% increase in micropore area versus ~8% increase in mesopore area). The calculated mesoporous parameters were 24 m^2/g and 0.04 cm^3/g higher for BT-*fsu*, with absolute values of 342 m^2/g and 0.448 cm^3/g. At the macroscopic level, the BT-*fsu* showed a total pore volume 11% higher than BT-*C, cf.* 0.562 and 0.508 cm^3/g.

In Figure 7 the differential pore volume versus the pore diameter calculated with the Horvath-Kawazoe model for BT-*C* and BT-*fsu* is plotted. BT-*fsu* displays a sharper pore diameter distribution and shifted to smaller pore diameters (*ca.* 0.05 Å) compared to BT-*C*. Thermal stress and sintering may be the cause of the peak broadening. The shift towards smaller pore sizes of the BT-*fsu* can be attributed to the different nature of the materials. BT-*fsu* remains in the NH_4-form [28] while BT-*C* is on the H-form; therefore the effective pore size for the Fenton-based material is smaller than for the calcined one.

3.5.3. Al-coordination

The Al-coordination was studied by ^{27}Al-MAS NMR. The spectra for various materials are displayed in Figure 8. The raw material shows a single resonance centred at *ca.* 50 ppm related to tetrahedrically coordinated framework-aluminium atoms [20]. BT-*fsu* shows no distortion in the Al atoms distribution after template removal, showing an identical pattern than the starting material (BT-*raw*). Contrariwise, BT-*C* displays, additionally to the framework Al, a shoulder (*ca.* 25 ppm) related to pentahedrically coordinated–Al [66] and a resonance at around 0 ppm ascribed to octahedrically-coordinated Al (AlO_6) [20]. Approximately 16% of the Al was driven off the structure (calculated as AlO_6) due to the thermal stress suffered during calcination.

4. Conclusions

The Hadamard design shows preliminary trends, with Fe concentration having the largest effect in the detemplation efficiency followed by H_2O_2 utilization and temperature. A thorough optimization study reveals that to achieve full detemplation, higher temperatures can compensate Fe concentration and H_2O_2 utilization. An interplay between H_2O_2 utilization and Fe concentration was also observed.

By understanding the interplay between relevant parameters, attractive reaction conditions for large-scale implementation were identified. If H_2O_2 needs to be minimized, optimal conditions are found at 88 °C, 30 ppm Fe and 15 mL H_2O_2/g, which means a relatively high solid concentration and low consumption of H_2O_2. When Fe should be limited in the final product composition, optimal conditions are obtained at 88 °C, 5 ppm Fe and 30 mL H_2O_2/g.

A kinetic study demonstrates that reaction time to get full detemplation can be reduced in several fashions: applying a higher Fe concentration, Fe-oxalates are more

effective than Fe-nitrate, especially under UV radiation, having the shortest reaction time of 5 h, at the applied conditions.

The protocol was scaled up to 100 times, with >99% detemplation efficiency. The resulting scaled material was structurally similar to the calcined counterpart based on similar Si/Al ratio and XRD pattern. Textural and Al coordination properties are more favourable compared to the calcined counterpart.

5. Acknowledgements

The 'Nederlandse Organisatie voor Wetenschappelijk Onderzoek' (NWO) is thanked for the financial support of the VIDI grant no. 10284. The industrial steering committee (Shell, DSM and Norit Nederland, now Cabot) and the Dutch Technology Foundation (STW) are acknowledged.

6. References

[1] D.W. Breck, Zeolite Molecular Sieves, Structure, Chemistry and Use, John Wiley & Sons, New York, 1974.

[2] J. Weitkamp, L. Puppe, Catalysis and Zeolites, Fundamentals and Applications, Springer, Berlin, 1999.

[3] J. Cejka, H. van Bekkum, A. Corma, F. Schueth (Eds.), Introduction to Zeolite Science and Practice, 3rd revised edition, Stud. Surf. Catal. 168, Elsevier, Amsterdam, 2007.

[4] R. Xu, W. Pang, J. Yu, Q. Huo, J. Chen, Chemistry of Zeolites and Related Porous Materials. Synthesis and Structure, John Wiley & Sons, Singapore, 2007.

[5] V. Valtchev, S. Mintova, M. Tsapatsis, Ordered Porous Solids: Recent Advances and Prospects, Elsevier, Amsterdam, 2009.

[6] J. Cejka, A. Corma, S. Zones, Zeolites and Catalysis: Synthesis, Reactions and Applications, Wiley-VCH, Weinheim, 2010.

[7] C.S. Cundy, P.A. Cox, Chem. Rev. 103 (2003) 663-701.

[8] J. Cejka, A. Corma, S. Zones, Zeolites and Catalysis: Synthesis, Reactions and Applications, Wiley-VCH, Weinheim, 2010, pp. 67.

[9] Burton, S. Zones, S. Elomari, Curr. Opin. Colloid In. 10 (2005) 211-219.

[10] Jackowski, S.I. Zones, S. Hwang, A.W. Burton, J. Am. Chem. Soc. 131 (2009) 1092-1100.

[11] R. Castaneda, A. Corma, V. Fornes, F. Rey, J. Rius, J. Am. Chem. Soc. 125 (2003) 7820-7821.

[12] Corma, F. Rey, J. Rius, M. Sabater, S. Valencia, Nature. 431 (2004) 287-290.

[13] Corma, M.J. Diaz-Cabanas, J. Luis Jorda, C. Martinez, M. Moliner, Nature. 443 (2006).

[14] J. Pérez-Pariente, J.A. Martens, P.A. Jacobs, Appl. Catal. 31 (1987) 35-64.

[15] M.A. Camblor, A. Mifsud, J. Pérez-Pariente, Zeolites. 11 (1991) 792-797.

[16] M.A. Camblor, A. Corma, S. Valencia, Micropor. Mesopor. Mater. 25 (1998) 59-74.

[17] T. De Baerdemaeker, B. Yilmaz, U. Mueller, M. Feyen, F. Xiao, W. Zhang, T. Tatsumi, H. Gies, X. Bao, D. De Vos, J. Catal. 308 (2013) 73-81.

[18] H. Zhang, B. Xie, X. Meng, U. Mueller, B. Yilmaz, M. Feyen, S. Maurer, H. Gies, T. Tatsumi, X. Bao, W. Zhang, D. De Vos, F. Xiao, Micropor. Mesopor. Mater. 180 (2013) 123-129.

[19] Yilmaz, U. Mueller, M. Feyen, S. Maurer, H. Zhang, X. Meng, F. Xiao, X. Bao, W. Zhang, H. Imai, T. Yokoi, T. Tatsumi, H. Gies, T. De Baerdemaeker, D. De Vos, Catal. Sci. Technol. 3 (2013) 2580-2586.

[20] E. Bourgeat lami, P. Massiani, F. Di Renzo, P. Espiau, F. Fajula, T. Courieres, Appl. Catal. 72 (1991) 139.

[21] Kiricsi, C. Flego, G. Pazzuconi, W.O. Jr. Parker, R. Millini, C. Perego, G. Bellussi, J. Phys. Chem. 98 (1994) 4627.

[22] P.J. Kunkeler, B.J. Zuurdeeg, J.C. van der Waal, J.A. van Bokhoven, D.C. Koningsberger, H. van Bekkum, J. Catal. 180 (1998) 234-244.

[23] J.A. van Bokhoven, D.C. Koningsberger, P. Kunkeler, H. van Bekkum, A.P.M. Kentgens, J. Am. Chem. Soc. 122 (2000) 12842-12847.

[24] C.W. Jones, K. Tsuji, T. Takewaki, L.W. Beck, M.E. Davis, Micropor. Mesopor. Mater. 48 (2001) 57-64.

[25] Gautier, M. Smaihi, New J. Chem. 28 (2004) 457-461.

[26] M. El Roz, L. Lakiss, V. Valtchev, S. Mintova, F. Thibault-Starzyk, Micropor. Mesopor. Mater. 158 (2012) 148-154.

[27] I. Melian-Cabrera, S. Espinosa, F.J. Garcia-Montelogo, F. Kapteijn, J.A. Moulijn, Chem. Commun. (2005) 1525-1527.

[28] I. Melian-Cabrera, F. Kapteijn, J.A. Moulijn, Chem. Commun. (2005) 2744-2746.

[29] I. Melian-Cabrera, F. Kapteijn, J.A. Moulijn, Catal. Today. 110 (2005) 255-263.

[30] L.L. Perez, M.J. Ortiz-Iniesta, Z. Zhang, I. Agirrezabal-Telleria, M. Santes, H.J. Heeres, I. Melian-Cabrera, J. Mater. Chem. A. 1 (2013) 4747-4753.

[31] Z. Zhang, D.L. Santangelo, G. ten Brink, B.J. Kooi, J.A. Moulijn, I. Melian-Cabrera, Mater Lett. 131 (2014) 186-189.

[32] Y. Xia, R. Mokaya, J. Phys. Chem B. 110 (2006) 9122-9131.

[33] Kecht, T. Bein, Micropor. Mesopor. Mater. 116 (2008) 123-130.

[34] N. Alam, R. Mokaya, J. Mater. Chem. 18 (2008) 1383-1391.

[35] F. Fan, Z. Feng, K. Sun, M. Guo, Q. Guo, Y. Song, W. Li, C. Li, Angew. Chem. Int. Edit. 48 (2009) 8743-8747.

[36] P. Wang, D. Yang, J. Hu, J. Xu, G. Lu, Catal. Today. 212 (2013).

[37] Wu, J. Liao, S. Fang, A.S.T. Chiang, Adsorption. 16 (2010) 69-74.

[38] Coronas, Chem. Eng. J. 156 (2010) 236-242.

[39] Hartmann, S. Kullmann, H. Keller, J. Mater. Chem. 20 (2010) 9002-9017.

[40] V. Valtchev, G. Majano, S. Mintova, J. Pérez-Ramirez, Chem. Soc. Rev. 42 (2013) 263-290.

[41] H. Xing, Y. Zhang, M. Jia, S. Wu, H. Wang, J. Guan, L. Xu, T. Wu, Q. Kan, Catal. Commun. 9 (2008).

[42] J. Lu, N. Liu, L. Li, R. Lee, Sep. Purif. Technol. 72 (2010).

[43] Xiao, J. Li, H. Jin, R. Xu, Micropor. Mesopor. Mater. 96 (2006).

[44] Y. Hu, Y. Zhang, Y. Tang, RSC Adv. 2 (2012) 6036-6041.

[45] D.Y. Khoo, H. Awala, S. Mintova, E. Ng, Micropor. Mesopor. Mater. 194 (2014) 200-207.

[46] Neyens, J. Baeyens, J. Hazard. Mater. 98 (2003) 33-50.

[47] W.Z. Tang, Physicochemical Treatment of Hazardous Wastes, CRC Press LLC, Florida, 2004.

[48] J.J. Pignatello, E. Oliveros, A. MacKay, Crit. Rev. Environ. Sci. Technol. 36 (2006) 1-84.

[49] Hedayat, W. Wallis, Ann. Stat. 6 (1978) 1184-1238.

[50] Baro, E. Sánchez, A. Delgado, A. Perera, C. Evora, J. Control. Release. 83 (2002) 353-364.

[51] R.J. Watts, M.D. Udell, P.A. Rauch, S.W. Leung, Hazard. Waste Hazard. 7 (1990) 335-345.

[52] Walling, Acc. Chem. Res. 8 (1975) 125-131.

[53] The CRC Handbook of Chemistry and Physics, 89th edition. ed., CRC Press, 2011.

[54] J. Perez-Ramirez, F. Kapteijn, J. Groen, A. Domenech, G. Mul, J. Moulijn, J. Catal. 214 (2003) 33-45.

[55] A.H. Oygarden, J. Perez-Ramirez, Appl. Catal. B-Environ. 65 (2006) 163-167.

[56] Hermankova, M. Hermanek, R. Zboril, Eur. J. Inorg. Chem. (2010).

[57] Hermosilla, M. Cortijo, C.P. Huang, Chem. Eng. J. 155 (2009) 637-646.

[58] Zhou, F. Wu, N. Deng, Chemosphere. 57 (2004) 283-291.

[59] M. Balmer, B. Sulzberger, Environ. Sci. Technol. 33 (1999) 2418-2424.

[60] Mazellier, B. Sulzberger, Environ. Sci. Technol. 35 (2001) 3314-3320.

[61] M. Thommes, Chem-Ing-Tech. 82 (2010).

[62] Prokesova-Fojokova, S. Mintova, J. Cejka, N. Zilkova, A. Zukal, Micropor. Mesopor. Mater. 92 (2006) 154-160.

[63] L. Wang, Z. Zhang, C. Yin, Z. Shan, F. Xiao, Micropor. Mesopor. Mater. 131 (2010) 58-67.

[64] J.C. Groen, L.A.A. Peffer, J. Perez-Ramirez, Micropor. Mesopor. Mater. 60 (2003) 1-17.

[65] K.S.W. Sing, D.H. Everet, R.A.W. Haul, L. Moscou, R.A. Pieroti, J. Rouquerol, T. Siemieniewska, Pure Appl. Chem. 57 (1985) 603-619.

[66] Duevel, E. Romanova, M. Sharifi, D. Freude, M. Wark, P. Heitjans, M. Wilkening, J. Phys. Chem. C. 115 (2011) 22770-22780.

Figures and Tables

Table 1. Detemplation conditions corresponding to the experimental design.

Parameters	**H1**	**H2**	**H3**	**H4**
P1: Detemplation temperature (°C)[a]	88	88	70	70
P2: H_2O_2 utilization (ml/g)	30	10	30	10
P3: Iron concentration (ppm)	60	0	0	60
Detemplation level (η^{TGA}, %)	99	19	25	37

a. The resolution of the Hadamard matrix is carried out using absolute temperature.

Table 2. Summary of the detemplation levels (η^{TGA}, %) as a function of temperature, Fe concentration (ppm), H_2O_2 utilization (ml/g) and reaction time (hours). Two types of commercial H_2O_2 were employed: stabilized, and *non*-stabilized (values in italics). Underlined values correspond to the detemplation efficiency based on CHN (η^C).

Temperature	**H_2O_2**	**Reaction**	**Iron concentration (ppm)**					
(°C)	**(ml/g)**	**time (h)**	**0**	**5**	**10**	**15**	**30**	**60**
RT	**10**	**24**	-	-	-	-	*25*	-
40	**30**	**8**	-	-	-	-	-	*32*
	30	**24**	*36*	-	*32*	-	*32*	*37*
	30	**48**	*22*	-	*30*	-	-	-
70	**10**	**24**	-	-	*31*	-	*31*	37
		30	-	-	-	-	*46*	-
	15	**24**	-	-	-	-	40	-
		30	-	-	*41*	-	*64*	-
	20	**24**	-	-	-	-	47/*56*	-
		30	-	-	*63*	-	*97*	-
	30	**11**	-	-	-	-	-	*99*
		24	25/*30*	-	*98*	45	100/*99*/96	100/*99*/98
		41	*32*	-	-	-	-	-
79	**10**	**24**	-	-	-	22	-	32
	15	**24**	-	-	-	73	40	65
	20	**24**	-	26	31	76	92	92
	30	**24**	22	32	89	91	95/99	96/96
88	**10**	**24**	19	-	-	-	-	-
	15	**24**	-	-	-	86	95/93	-
	20	**24**	29	93	93	97/92	-	-
	30	**24**	48	98/97	-	-	-	99

Table 3. Summary of the detemplation conditions, CHN elemental analysis (*wt.*%), Si/Al and Fe composition for the optimal and reference materials.

Material	Si/Al	Fenton conditions			Elemental analysis / *wt.* %				Fe^{ADS} / %	η^C / %
		H_2O_2 ml/g zeolite	T / °C	[Fe] / ppm	C	H	N	Fe		
BT-*raw*	13.5 [a]	-	-	-	10.4	2.1	1.6	-	-	0
BT-*C*	13.1	-	-	-	0.0	0.3	0.0	0.01	-	100
BT-*f*	12.4	30	70	30	0.4	1.1	1.5	0.08	64	96
BT-*fsu*	12.8	30	70	30	<0.1	1.3	1.3	0.10	83	>99

[a]: Commercial specifications.

Table 4. Summary of the porosity parameters calculated from the high-resolution argon physisorption isotherms at –186.2 °C.

Material	S_{BET} m^2/g	S_{μ}^{t-plot} m^2/g	S_{MESO}^{t-plot} m^2/g	V_T cm^3/g	V_{μ}^{t-plot} cm^3/g	V_{MESO}^{t-plot} cm^3/g
BT-*C*	566	248	318	0.508	0.097	0.411
BT-*fsu*	628	286	342	0.562	0.114	0.448

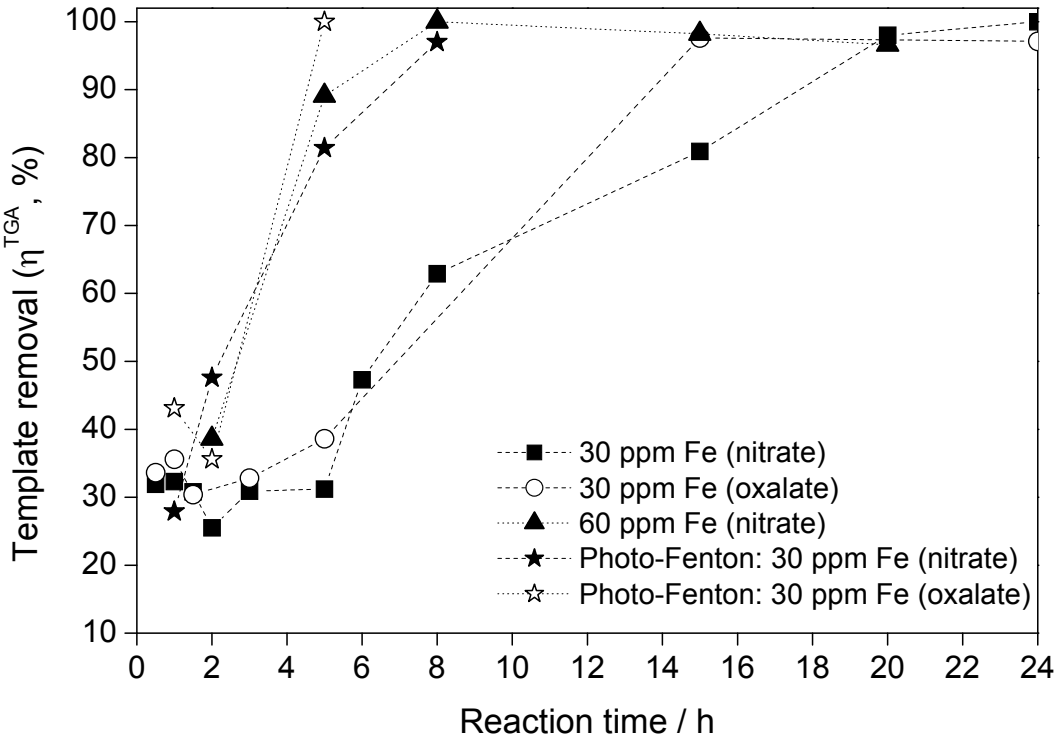

Figure 1. Kinetic study under dark and UV-light conditions. Template removal (η^{TGA}, %) as a function of the reaction time using 30 and 60 ppm of Fe. Fe^{III}-nitrate and Fe^{III}-oxalate were used as iron sources and the reaction temperature was kept constant at 70 °C. The use of UV-Vis light (5.5 W) was applied for 30 ppm Fe^{III}-nitrate and Fe^{III}-oxalate.

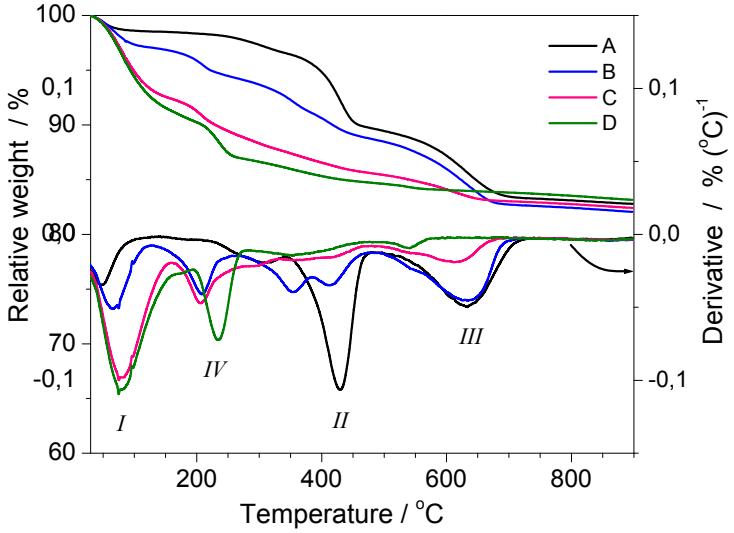

Figure 2. TGA and DTGA patterns of the partially Fenton detemplated materials at different H_2O_2 utilisation: (**B**) 10 mL/g; (**C**) 15 mL/g; and (**D**) 30 mL/g at 79 °C and 60 ppm of Fe. BT-*raw* was added for comparison (**A**).

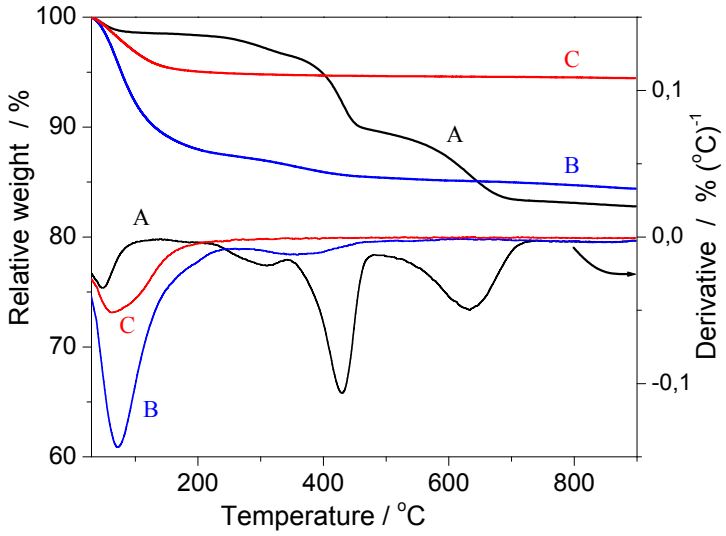

Figure 3. TGA/DTGA patterns of the raw beta zeolite (**A**, BT-*raw*), the scaled-up Fenton detemplated (**B**, BT-*fsu*) and the calcined (**C**, BT-*C*)

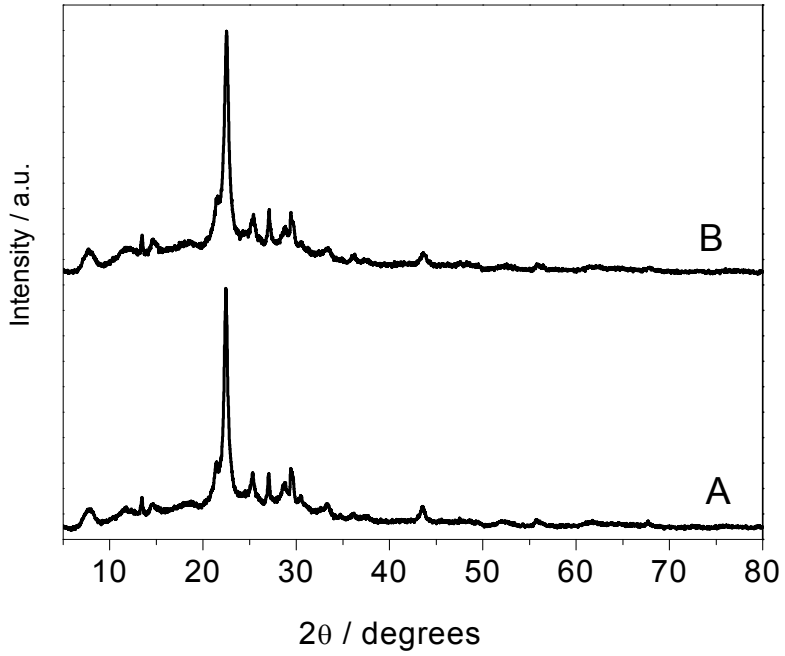

Figure 4. XRD patterns for the scaled-up Fenton detemplated (**A**, BT-*fsu*) compared to the calcined counterpart (**B**, BT-*C*).

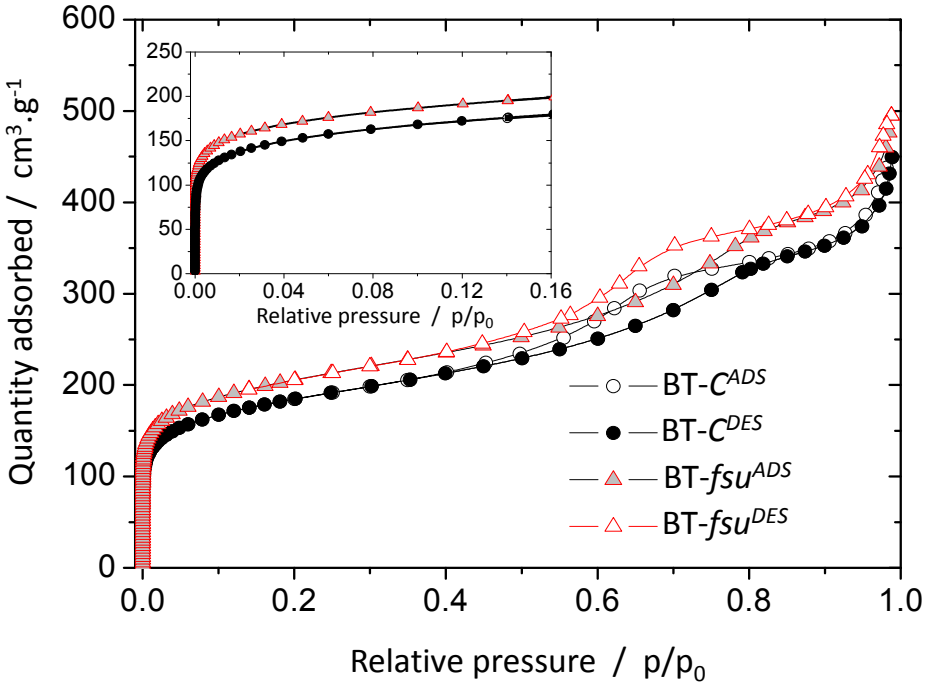

Figure 5. High-resolution Argon physisorption isotherms at –186.2 °C for the calcined and scaled-up Fenton detemplated counterpart. The superscript in the sample codes indicates whether it is an adsorption or desorption branch.

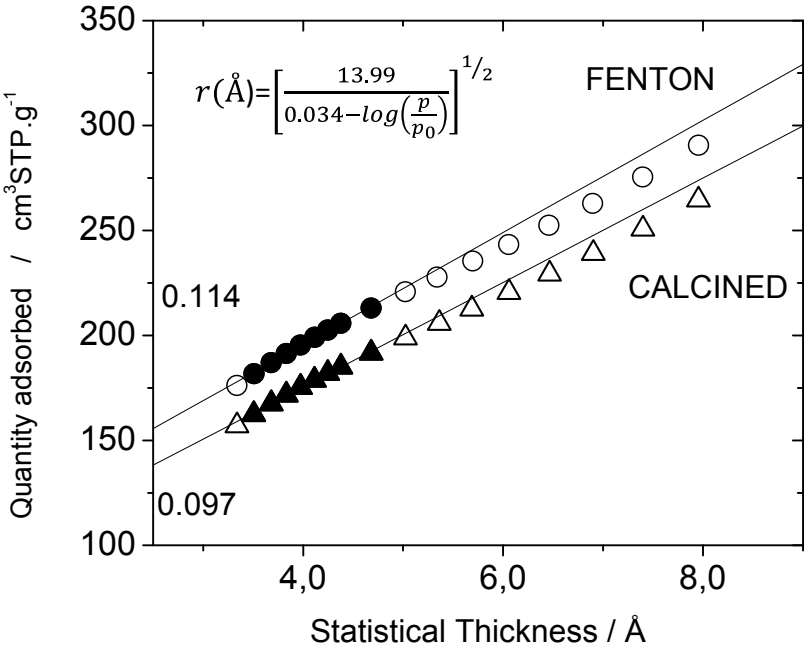

Figure 6. Harkins and Jura *t*-plot derived from the LPHR-Argon adsorption (–186.2 °C) of Fenton detemplated (BT-*fsu*) and calcined Beta zeolite (BT-*C*).

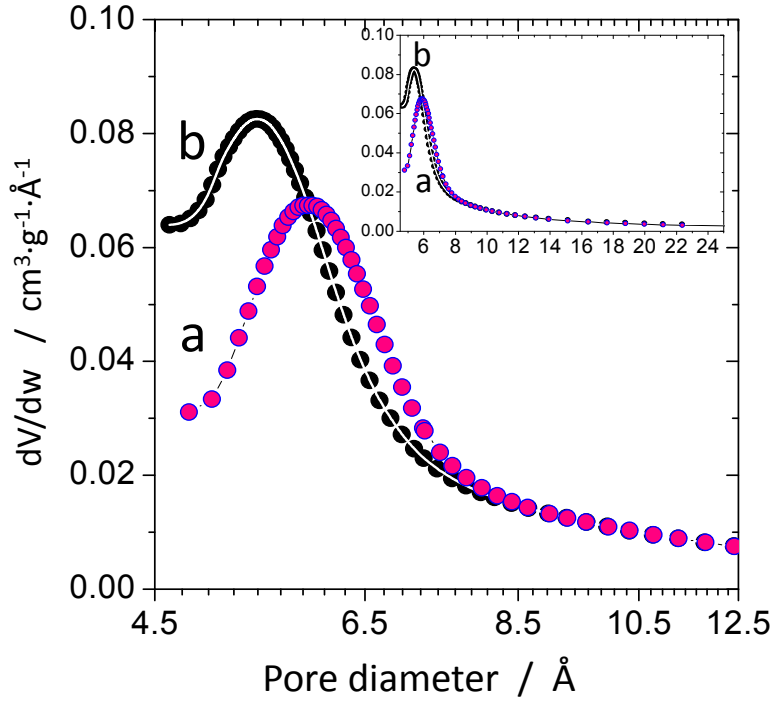

Figure 7. Horvath-Kawazoe differential pore volume for the calcined (**a**) and scaled-up Fenton detemplated (**b**), applied to the LPHR isotherms (Ar, –186.2 °C).

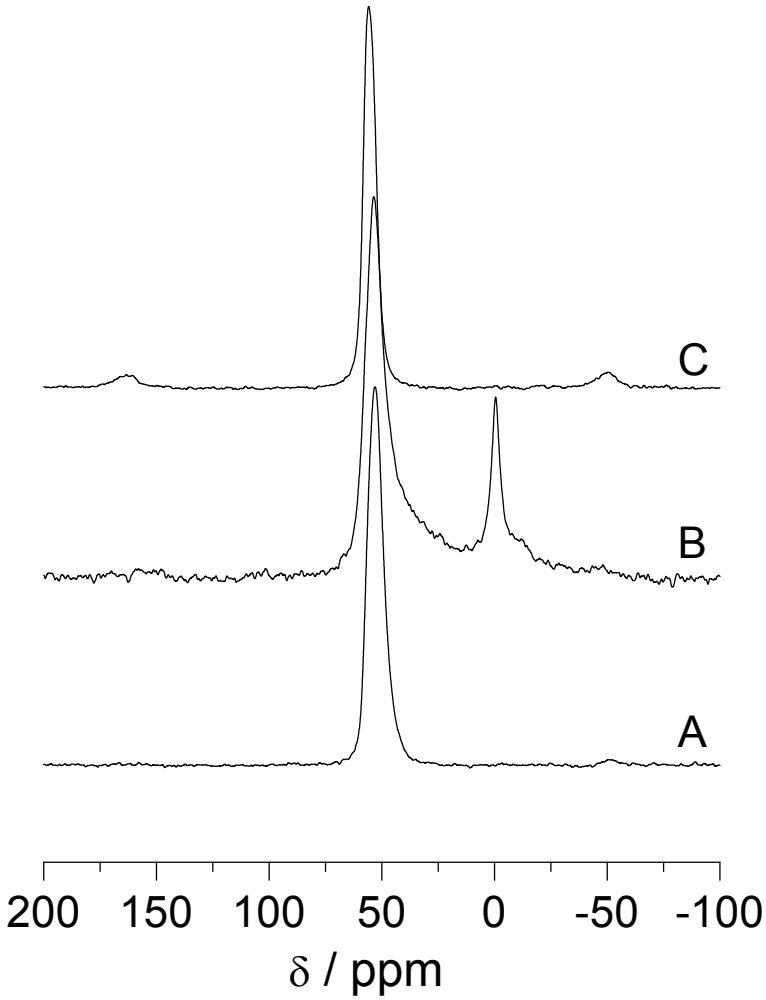

Figure 8. ^{27}Al MAS NMR spectra for the raw material (**A**), calcined (**B**) and scaled-up Fenton detemplated (**C**).

Electronic Supporting information

Fenton chemistry-based detemplation of an industrially relevant microcrystalline beta zeolite. Optimization and scaling-up studies.

María J. Ortiz-Iniesta and Ignacio Melián-Cabrera*

Chemical Reaction Engineering, Institute of Technology & Management, University of Groningen, Nijenborgh 4, 9747 AG Groningen, The Netherlands.

* Corresponding Author:

i.v.melian.cabrera@rug.nl (Ignacio Melián Cabrera)

1. Supporting information.

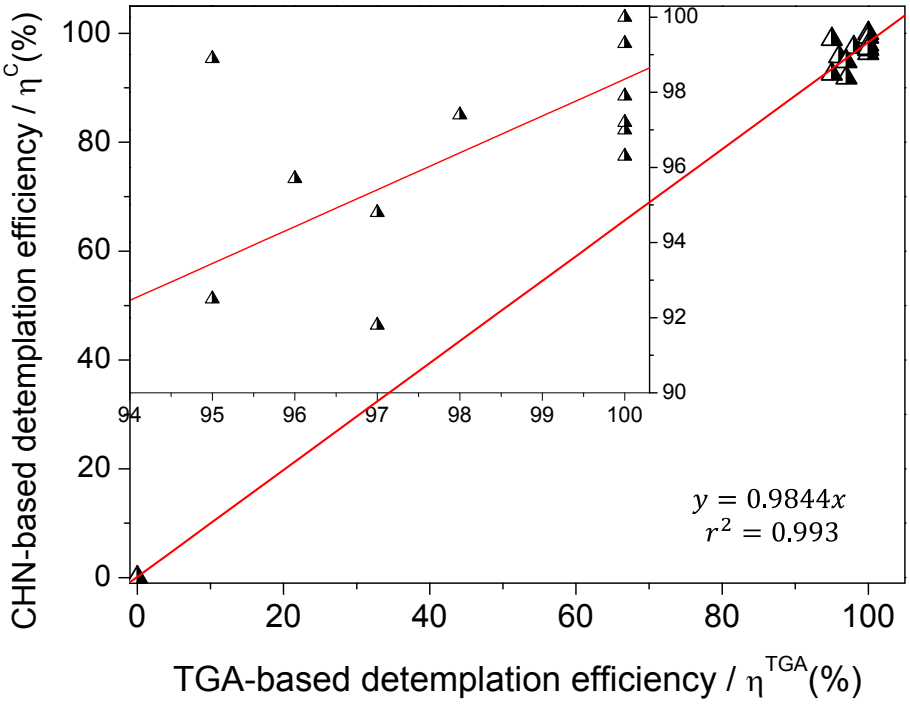

Figure S-1. TGA based detemplation efficiency (%) vs. CHN based detemplation efficiency (%); the equation of the lineal correlation is shown.